PNAS RESEARCH ARTICLE | APPLIED BIOLOGICAL SCIENCES ENGINEERING

# AI-boosted and motion-corrected, wireless near-infrared sensing system for continuously monitoring laryngeal muscles

Yihan Liu[a], Arjun Putcha[a], Gavin Lyda[b], Nanqi Peng[c], Salil Pai[c], Tien Nguyen[a], Sicheng Xing[c], Shang Peng[d], Yiyang Fan[e], Yizhang Wu[a], Wanrong Xie[a], and Wubin Bai[a,1]

Edited by John Rogers, Northwestern University, Evanston, IL; received May 30, 2024; accepted October 16, 2024

**Neuromuscular diseases pose significant health and economic challenges, necessitating innovative monitoring technologies for personalizable treatment. Existing devices detect muscular motions either indirectly from mechanoacoustic signatures on skin surface or via ultrasound waves that demand specialized skin adhesion. Here, we report a wireless wearable system, Laryngeal Health Monitor (LaHMo), designed to be conformally placed on the neck for continuously measuring movements of underlying muscles. The system uses near-infrared (NIR) light that features deep-tissue penetration and strong interaction with myoglobin to capture muscular locomotion. The incorporated inertial measurement unit sensor further decouples the superposition of signals from NIR recordings. Integrating a multimodal AI-boosted algorithm based on recurrent neural network, the system accurately classifies activities of physiological events. An adaptive model enables fast individualization without enormous data sources from the target user, facilitating its broad applicability. Long-term tests and simulations suggest the potential efficacy of the LaHMo platform for real-world applications, such as monitoring disease progression in neuromuscular disorders, evaluating treatment efficacy, and providing biofeedback for rehabilitation exercises. The LaHMo platform may serve as a general noninvasive, user-friendly solution for assessing neuromuscular function beyond the anterior neck, potentially improving diagnostics and treatment of various neuromuscular disorders.**

neuromuscular diseases | wearable near-infrared spectroscopy | AI | hardware AI

## Significance

Neuromuscular diseases significantly impact health and quality of life globally, creating a need for advanced monitoring technologies. Our research presents an AI-boosted, wireless sensing system Laryngeal Health Monitor (LaHMo) that uses near-infrared light and motion sensors to monitor muscle activity in the neck continuously. This system integrates a dual-modality algorithm for precise event classification and adapts quickly to individual users. By enabling real-time, noninvasive monitoring of conditions like dysphagia and dysphonia, LaHMo offers possibilities for tracking disease progression, evaluating treatment efficacy, and aiding rehabilitation.

Neuromuscular diseases (NMDs), characterized by progressive muscle function deterioration, pose significant healthcare challenges worldwide. They profoundly impact patient mobility, quality of life, and economic burden, especially in the postpandemic era (1, 2). Managing NMDs is costly, encompassing financial costs, lost productivity, and psychological toll on patients and families (3–5). Muscle-tracking technology, combining biosensors and analytical algorithms, has emerged as a promising solution for real-time monitoring of specific muscular units (6, 7). This field holds immense potential for creating innovative treatments for NMDs and advancing the development of user-friendly cybernetic interfaces (8, 9). The anterior neck region comprises both intrinsic and extrinsic laryngeal muscles, each with distinct physiological roles (10–13). The intrinsic muscles, including the thyroarytenoid and cricothyroid muscles, are primarily responsible for modulating tension and length of the vocal cords, facilitating phonation. In contrast, the extrinsic muscles, such as the sternohyoid and thyrohyoid, are involved in positioning and stabilizing the larynx during swallowing and respiration. Dysfunction in these muscle groups can manifest as conditions like dysphonia, which often stems from intrinsic muscle impairment affecting vocal cord vibration, and dysphagia, which may involve a complex interplay of both intrinsic and extrinsic muscle dysfunction affecting the coordination of swallowing (14, 15). Additionally, abnormal activity in these muscles can be associated with persistent post-COVID dry cough, where monitoring muscle function can provide insights into the extent and impact of these symptoms (16, 17). Moreover, the frequent and involuntary occurrence of throat clearing, and dry cough can be indicative of dystussia, a cough dysfunction characterized by an impaired cough reflex or coordination, potentially leading to ineffective airway clearance and respiratory complications. Monitoring these symptoms with precision could be crucial for the early detection and management of dystussia, thus enhancing patient outcomes (18). A nuanced examination of the intrinsic and extrinsic laryngeal muscle groups is essential for accurate diagnoses and therapeutic interventions, as well as for evaluating the progression and treatment of post-COVID conditions.

Existing muscle tracking technologies primarily rely on ultrasonic sensors (19–21), near-infrared spectroscopy (NIRS) (22–24), electromyography (EMG) (25–27), inertial

Author affiliations: [a]Department of Applied Physical Sciences, University of North Carolina, Chapel Hill, NC 27599; [b]Department of Physics and Astronomy, University of North Carolina, Chapel Hill, NC 27599; [c]Joint Department of Biomedical Engineering, University of North Carolina/North Carolina State University, Chapel Hill, NC 27599; [d]Department of Computer Science, University of North Carolina, Chapel Hill, NC 27599; and [e]Department of Biostatistics, University of North Carolina, Chapel Hill, NC 27599

Author contributions: Y.L. and W.B. designed research; Y.L., G.L., N.P., S. Pai, T.N., S. Peng, and W.B. performed research; Y.L. contributed new reagents/analytic tools; Y.L., A.P., S.X., Y.F., Y.W., and W.X. analyzed data; and Y.L. wrote the paper.

Competing interest statement: The University of North Carolina at Chapel Hill (No. 63/717,662: filed on Nov. 7, 2024) filed a provisional patent application, titled "Method, apparatuses, and systems for continuous muscle monitoring and health status prediction", surrounding this work, where W.B. and Y.L. are the co-inventors. The remaining authors declare no competing interest.

This article is a PNAS Direct Submission.



[1]To whom correspondence may be addressed. Email: wbai@unc.edu.

This article contains supporting information online at https://www.pnas.org/lookup/suppl/doi:10.1073/pnas.2410750121/-/DCSupplemental.

Published December 9, 2024.

measurement units (IMU) (28, 29), and mechanoacoustic (MA) sensors (30–32), which have several limitations. Ultrasonic sensors typically necessitate a specialized adhesive layer to effectively transmit ultrasound waves, which can be inconvenient for long-term monitoring. Signals collected from EMG sensors have limited spatial resolution due to inherent noise from electrode crosstalk, electromagnetic interference, and electrocardiographic artifacts. IMU-based muscle trackers suffer from signal drift over time and require sophisticated algorithms to interpret complex muscle movements. MA sensors require a high computational load for signal analysis and are not ideal for large-area, spatially resolved signal detection. NIRS sensors rely on strong attachment between the sensor and the skin to ensure LED-tissue coupling, thus making them prone to motion artifacts and compromising the wearing comfort. However, there is potential in that ultrasonic and NIRS sensors collect signals in the temporal domain capable of monitoring short- and long-term muscle activities, such as swallowing and static exercises, along with IMU, EMG, and MA sensors collecting signals in the frequency domain capable in distinguishing dry cough, talking, and dynamic exercises. Integrating these sensors into a single platform may hold great promise via an AI algorithm in leveraging their respective capabilities while mitigating the limitations.

Here, we report a wireless, wearable, multimodal muscle-tracking system, named Laryngeal Health Monitor (LaHMo). The device features four NIRS sensors, to track muscle activity during various physiological events, and a synchronized IMU sensor, to audit device global motion serving as a reference for counteracting motion artifacts. The hybrid sensing approach is enhanced with an AI-driven platform and a wireless data collection system, offering improved portability and instantaneous data analysis capabilities. This integration of AI models surpasses traditional methods by providing more accurate predictions and comprehensive insights into muscle behavior, thus enabling more precise monitoring and treatment strategies. A Monte Carlo simulation and two simultaneous gold standard tests based on EMG and videostroboscopy validate the NIRS technology in tracking muscles of the anterior neck area, visualizing the penetration depth of the sensor (33, 34). Long-term on-body tests demonstrate the capability of LaHMo in continuously monitoring laryngeal muscle activity during various physiological events, including deep breathing, coughing, swallowing, and exercise. High-level physiological indicators, including respiratory health and exercise intensity, draw real-time LaHMo measurements into instant clinically relevant feedback via the AI models, thus offering advanced point-of-care diagnostics. These tests showcase its potential for real-world applications, such as tracking disease progression, evaluating treatment efficacy, and providing biofeedback for physical rehabilitation and sports performance monitoring related to deep muscular tissue (35, 36). The LaHMo platform may establish a broadly applicable solution for continuous, noninvasive monitoring of muscular locomotion, with the potential to improve the diagnosis and treatment for a broad range of NMDs.

## Results

**Design Concept of LaHMo Platform.** Fig. 1*A* illustrates the utility of a LaHMo. The ergonomic design of the LaHMo patch allows conformal attachment onto the anterior neck region with minimal discomfort. The patch transmits data to a cloud server capable of real-time AI analysis. The analysis of LaHMo signals could enable continuous monitoring of long-COVID symptoms of coughing, dysphagia, and dysphonia. Those collected data streaming in real-time inform clinicians and caregivers for deeper interpretations and informed decisions for personalized therapeutics. Fig. 1*B* provides an exploded view of a LaHMo patch which features a flexible design for both ergonomic fit and integrated functionality. The LaHMo patch uses two stretchable serpentine hinges to connect two smaller daughter islands with its main island that contains arrays of small holes for good air permeability (*SI Appendix*, Fig. S1). The sensors on the main island include i) an IMU module (LSM6DSOX, STMicroelectronics) for motion tracking, which features a detect range of ±16 g for acceleration and ±2,000 degree per second (dps) for angular rate, at a sample rate of 1.6 kHz, ii) two NIRS sensors, each consisting of one NIR light emitting diode (LED) (SFH 4043, Osram) and one photodiode (PD) (VEMD1060X01, Vishay) for muscle activity monitoring. Injection of NIR light into the skin allows absorption and scattering primarily from the muscle tissue beneath the sensor, as myoglobin richly contained in muscles shows strong absorption in NIR. Part of the backscattered light post to the light–tissue interaction can reach a nearby PD which generates corresponding signals that reflect muscular modulation. The on-board distance between each pair of PD and LED is set to 3.5 mm, which has shown optimized sign correspondence and signal-to-noise ratio (6, 33). The key integrated circuits (ICs) on the main island include i) a Bluetooth Low Energy (BLE) microcontroller unit (MCU) (ESP32-C3FH4, Espressif) to support data acquisition from the sensors, computation tasks, and wireless communication capabilities, ii) an analog-to-digital converter (ADC) (ADS1115, Texas Instruments) featuring a 16-bit resolution for 4 channels to handle data coming from the photodiodes before transmitting to the MCU, iii) two operational amplifiers (Op Amp, TLV9002IDSGT, Texas Instruments) that act as transimpedance amplifiers to preprocess the photovoltages output by the photodiodes, iv) two low dropout (LDO) linear regulators (ADP7118ACPZN-R7, Analog Devices) for power noise removal. Furthermore, the two daughter islands also consist of one NIRS sensor each.

The flexible serpentine hinges are designed to ensure not only the continuity of the electrical connectivity between the islands but also a flexible fit that conforms to the neck's profile while maintaining structural integrity (*SI Appendix*, Fig. S2). A removable lithium-ion battery (Engpow, 150 mAh) is used to power the whole patch, and it can support the device running for 4 h or longer if using intermittent sleep mode (*SI Appendix*, Fig. S3) (37). Fig. 1*C* displays an actual device worn by a subject on the anterior neck to demonstrate the true-to-size perspective of the LaHMo patch. The compact and unobtrusive design shows that the patch can be used in everyday settings without hindering the normal activities of the user. A detailed block diagram illustrating the operational mechanism of the proposed LaHMo platform appears in Fig. 1*D*. The biosensor section of the LaHMo platform serves as the foundation for data acquisition and initial processing. This includes the communication between the microcontroller and other on-board sensors. Specifically, the LEDs are programmed through the programmable analog outputs of the MCU, while the NIRS signal is sent to the external ADC module before reaching the Inter-Integrated Circuit ($I^2C$) interface of the MCU, together with the data from the IMU, which is then processed through a Madgwick filter (*SI Appendix*, Note S1). The AI analysis section outlines the algorithms and computational processes that interpret the collected data. First, a BLE client, which can be either a smartphone/watch or a personal computer, acquires the wirelessly transmitted data and presents the processed data in an

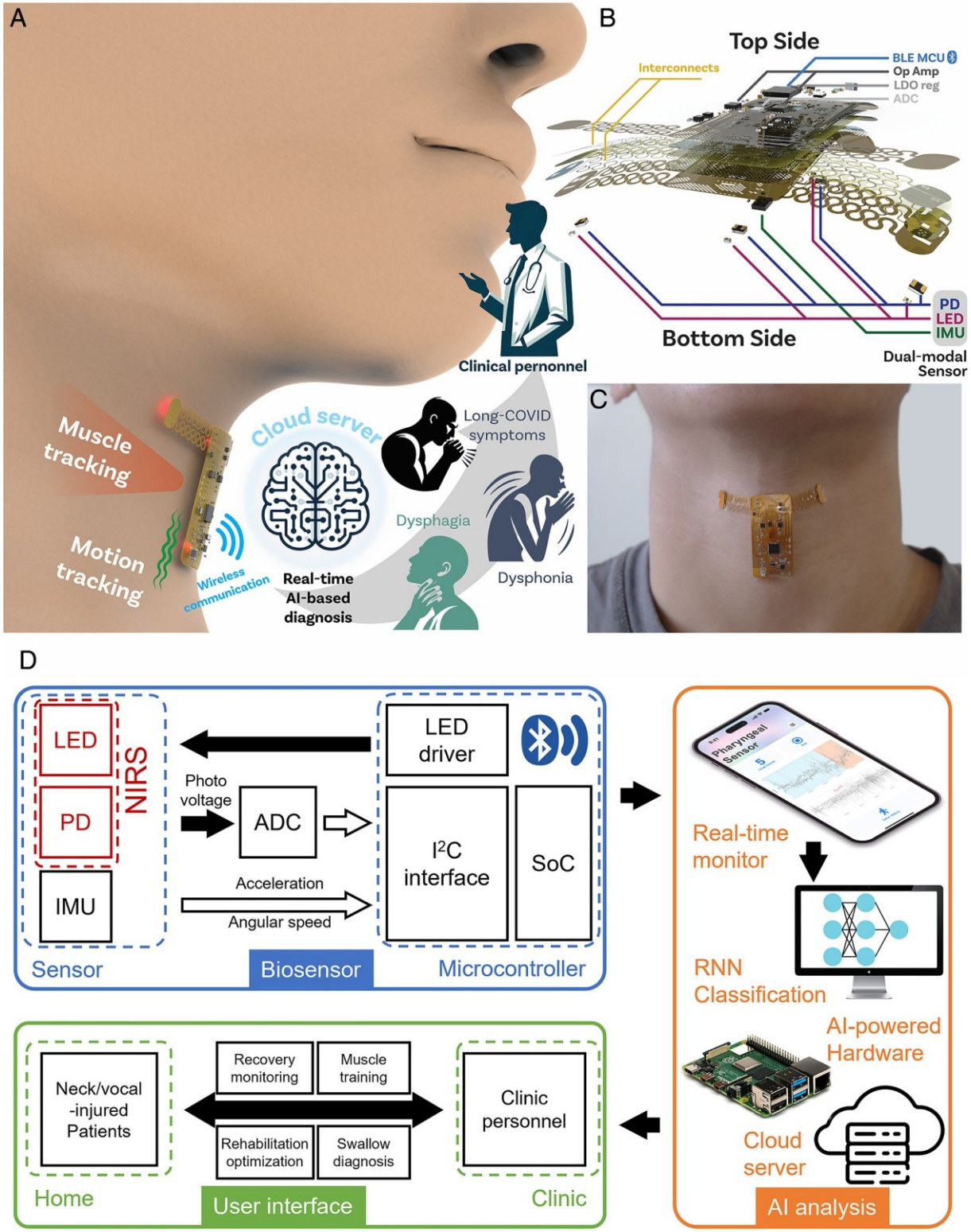


**Fig. 1.** Design concept of the LaHMo. (*A*) Schematic illustration of a LaHMo patch deployed onto the laryngeal anterior area for muscular monitoring, symptom tracking, and recovery evaluation. Right diagram: working flowline of the LaHMo on the laryngeal anterior area and the targeted applications. The LaHMo platform features onsite continuous muscle tracking over the laryngeal anterior area and wireless communication coupled with AI boosted predicting analysis that classifies neck movement, swallow behavior, respiratory symptoms, and others, serving as diagnostic basis for clinical decision-making and precision treatment. (*B*) Exploded view of a LaHMo patch. The patch uses a serpentine hinge to enable mechanical foldability, facilitating both ergonomic fit and function. The hinge connects the main and daughter islands into a single flexible printed circuit board (fPCB), with the former running integrated circuits, including a microcontroller, an analog-to-digital converter, an operational amplifier, two of the four NIRS sensors, and an IMU, while the latter hosts the other two NIRS sensors. (*C*) Image of a LaHMo patch deployed onto the neck. (*D*) Block diagram showing the operational flow of the LaHMo system. A BLE client (e.g., a smartphone) receives wirelessly transmitted data from a LaHMo patch and presents it in an accessible format for immediate review. The data is further analyzed with a pretrained RNN designed to detect and classify physiological events indicative of laryngeal health. This AI-powered analysis can be conducted in embedded systems or cloud servers. Finally, the users utilize the analyzed data for various medical and health applications. The LaHMo platform could facilitate a bidirectional flow of dynamic and effective interactions between caregivers and receivers.

accessible format for immediate review. Then, further data analysis relies on a pretrained recurrent neural network (RNN) classification system. This AI-powered analysis can occur either on the edge via embedded systems or in the cloud, with the latter providing the computational power needed for more complex interpretations. Finally, the human interface section shows the core of the LaHMo platform, emphasizing its practical application in various scenarios ranging from muscle tracking, swallow training, vocal training, surgical recovery monitoring, and others. For patients with neck injuries at home, the LaHMo platform monitors recovery progress and offers suggestions for laryngeal muscle training and rehabilitation optimization based on the determination from the clinic end. In a clinical setting, the LaHMo platform provides healthcare professionals with smart diagnosis capabilities based on the comprehensive statistics acquired from the patient in real time. This bidirectional flow of information fosters a dynamic interaction between patients and clinicians, promoting a more engaged and informed healthcare experience with personalized precision.

**Data Preprocessing Approaches at Various Physiological Events.** Data preprocessing improves visualization of muscle activity and prepares for continuous condition classification, both in real time. Here, we make use of a multiprocessing strategy to analyze, visualize, and store acquired data in real time (Fig. 2, and Movie S1). Fig. 2*A* demonstrates the strategic placement of the NIRS sensors on the neck, highlighting the top left, top right, central, and bottom positions. These locations are chosen for their proximity to key laryngeal muscles, including the sternohyoid muscle and mylohyoid muscle, involved in various physiological functions (swallowing, cough, speech, respiration, and others). Fig. 2*B* details the orientation axes—pitch, yaw, and roll—utilized in the data collection process, providing a three-dimensional perspective on how neck movements are recorded. Fig. 2*C* showcases a LaHMo patch highlighting the relative locations of respective sensors, which correlates with the sensing areas shown in Fig. 2*A*.

The *SI Appendix*, Fig. S4 illustrates the sequential flow of data processing concurrent with the detection of signals by the LaHMo patch. The initialization stage includes three processes storage, analysis, and visualization. The storage process creates a tabular database upon instantiation and prepares to receive and store serial data according to a known set of keys. The analysis process starts acquiring serial data and stores new data in a temporary buffer. The acquisition of data is accomplished using a custom software and user interface, named BTViz, to handle Bluetooth connection events, store acquired data in a buffer, and visualize acquired data. At each minute interval, this temporary buffer stores a tabular database in the storage process for filtering. These preprocessed data are then sent to a visualization process to be plotted in real time using BTViz for further analyzing and visualization. Fig. 2*D* presents a comprehensive analysis of physiological events across a spectrum of laryngeal muscle motion frequencies, each row corresponding to a specific sensor location and each graph demonstrating the signal detected during the activity at each location. The left four columns represent the low-frequency activities we desire to investigate: deep breathing, swallowing, dry coughing, and throat clearing. The right two columns are the high-frequency activities, categorized as aerobic and anaerobic workouts, that we aim to decouple from the low-frequency activities. enabling the identification of unique signal patterns associated with various neck activities, allowing for further differentiation between voluntary movements and involuntary muscle activity.

**Neural Network Classification of Preprocessed Windows.** Neural network classification of preprocessed windows is designed to decode natural physiological activities engaging the anterior neck muscle group, often accompanied by head motions. The

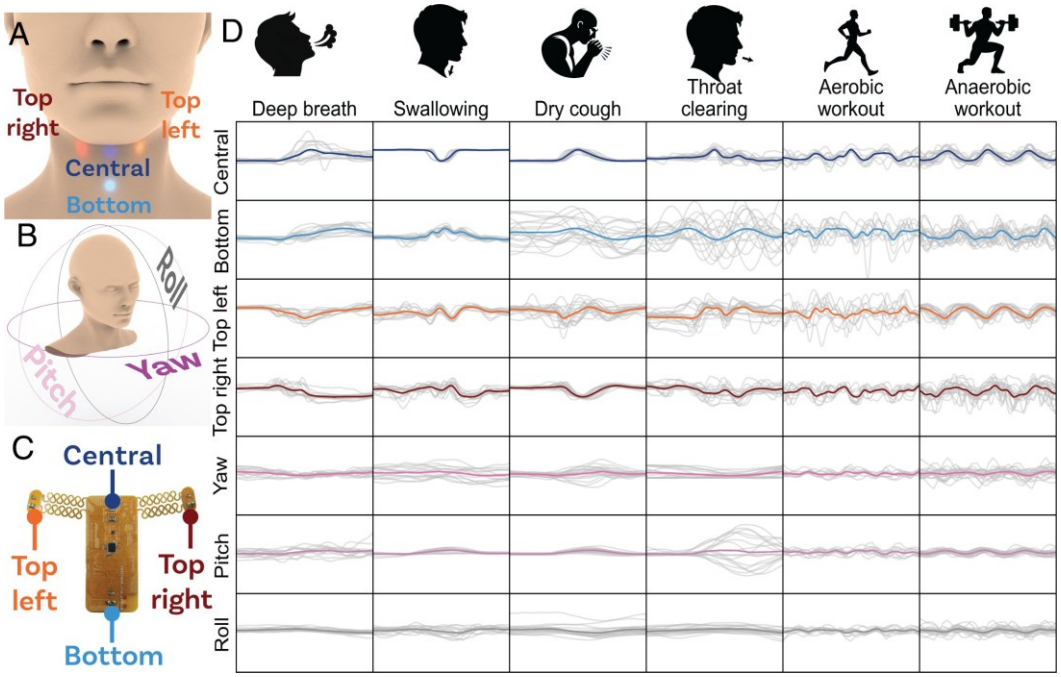


**Fig. 2.** Signal preprocessing and representative correlation with physiological events. (*A*) Schematic illustration indicating the corresponding sensing locations of the NIRS sensors in a LaHMo patch, highlighted with the central area (blue), bottom area (light blue), *Top Left* area (orange), and *Top Right* area (red), respectively. (*B*) Schematic illustration indicating dimensional parameters acquired from the embedded IMU, including the yaw (purple), pitch (pink), and roll (gray) Euler angles, respectively. (*C*) Image of a LaHMo patch showing the corresponding position of the NIRS sensors. (*D*) Representative preprocessed data from a repetitive test, on physiological events including deep breath, swallowing, dry cough, throat clearing, aerobic workout, and anaerobic workout. The preprocessed data feed into AI models for further analysis.

integration of IMU and NIRS sensors harnesses a comprehensive view, capturing both muscle activities (MA) and head motions (HM). This dual modality is central to the development of our classification algorithm, aiming to extract MA and HM information against the backdrop of ambient signals. Recurrent neural networks (RNNs) are known to be good at grasping the trend and making predictions based on the development of the temporal slices (38, 39). Here we develop a dual-channel RNN based on gated recurrent units (GRU), named dual-GRU, allowing for dedicated processing of IMU and NIRS data, enhancing its ability to stand against motion artifacts and extract relevant features (*SI Appendix*, Note 5). *SI Appendix*, Fig. S5 shows the comparison between the LaHMo signals acquired for a cough event while standing still and walking, demonstrating the system capability to filter out motion-induced artifacts during walking. While NIRS data show increased noise during walking due to physical motion, the IMU data capture characteristic patterns of movement that the dual-GRU model utilizes to isolate and remove those artifacts. We have carried out a systematic comparison between the developed dual-GRU and various other RNN architectures based on fully recurrent neural networks (FRNN), long short-term memory (LSTM), and gated recurrent units (GRU) along with their bidirectional variants (BiFRNN, BiLSTM, and BiGRU) that connect two hidden layers of opposite directions, to demonstrate the enabling capabilities offered by the dual-GRU.

Here, the preprocessed data (Fig. 2*D*) is used to construct the dataset used for training and validating the models. Fig. 3*A* elucidates the performance difference between the proposed dual-channel RNN (dual-RNN) and a normal monochannel RNN (mono-RNN). In a mono-RNN architecture, the preprocessed data [with a dimension of (1, 3000, 7)] will be sent directly to the hidden layer [with a dimension of (1, 3000, 140)] that updates for every time point. The hidden layer is then sent to a fully connected (FC) layer (1, 5) before finally outputting the result via a SoftMax (SM) layer. Generally, to gain the best performance of the neural network, this method requires normalization in the preprocessing to avoid a biased weight toward one of the two types of sensors. This not only brings more parameters to fine-tune but also reduces the universality and robustness of the model. Conversely, the dual-RNN architecture employs two parallel hidden layers, each dedicated to processing data from one of the two distinct sensor types. Specifically, the collected seven-channel data are first divided into the four-channel for photovoltage signals and the three-channel for Euler-angle information before being processed individually through the two designated RNN layers. The outputs of these two RNN layers are then concatenated and sent to the FC and SM layers. Fig. 3 *B*–*D* showcases the representative results of the trained RNNs. To emphasize the significance of combining the IMU and NIRS data, the results of the biased model utilizing data from one of the sensors, are also displayed, as PV-biased and IMU-biased, to compare segregated and integrated data (Fig. 3*B*). Furthermore, the performances of FRNN, LSTM, and GRU and their bidirectional variants (BiFRNN, BiLSTM, and BiGRU) are also discussed for the optimization of the architecture, with the loss and accuracy curves of their training and testing datasets presented by *SI Appendix*, Fig. S6. Finally, to prevent the potential training bias that comes from the way the involved dataset is selected from the whole data pool during the training process, a k-fold cross-validation is implemented to validate the model statistically. Fig. 3 *B*–*G* shows a series of evaluations on 24 different RNN architectures based on FRNN, LSTM, and GRU, with a particular focus on the dual-GRU model. Fig. 3*B* shows the reduction of the cross-entropy loss of all eight types of GRU models (PV-biased GRU, PV-biased BiGRU, IMU-biased GRU, IMU-biased BiGRU, mono-GRU, mono-BiGRU, dual-GRU, and dual-BiGRU), and the training performances for FRNN and LSTM are shown in *SI Appendix*, Fig. S7. During a 400-epoch training process, all eight models show a typical reduction-converge shape, and a good early stopping (ES) point can be observed at epoch = 200. The trends of the plots show a significant difference between the sensor-biased models and the comprehensive models that make use of both modalities of the LaHMo patch. Specifically, the mono- and dual-RNNs display a much steeper learning curve and converge points better than their competitors, who use only one modality (*SI Appendix*, Fig. S8). This observation promotes the advantage of synergizing NIRS and IMU detectors, compared to using only one of the two types of sensors. However, the bidirectional feature does not bring about much of a difference in the learning rate and the final loss function. Fig. 3*C* highlights the accuracy development among the train and test datasets between dual-GRU and dual-BiGRU. The results show that dual-GRU has a higher accuracy for both train and test datasets compared to dual-BiGRU, and the overfit problem is more severe for dual-BiGRU. This observation confirms that the bidirectional RNNs offer performance comparable with the conventional RNNs. Fig. 3*D* and *SI Appendix*, Figs. S9–S11 show the confusion matrices of the dual-GRU and other networks in the preprocessed data. For dual-GRU, it achieves accuracies of 1.00 for deep breathing, 0.92 for dry coughing, 0.92 for throat clearing, 0.90 for swallowing, 1.00 for aerobic exercising, and 0.91 for anaerobic exercising, with these events respectively represented by labels 0-5 in the confusion matrix.

Fig. 3*E* shows the event recognition during a continuous dry cough scenario, with the top half of the plot showing the NIRS readings, and the bottom half of the plot showing the IMU measurements. The green markers show the manually labeled MA events. The crosses and dots are manually labeled samples in the train and test datasets in one possible split, respectively. The red crosses label the recognized MA events by the trained GRU model. *SI Appendix*, Fig. S12 provides more related examples of other MA and HM events. Dry coughs were one such MA event, with the PD responses from various coughing patterns, including continuous, random, and separate, differentiated by the interval between cough events, successfully visualized (*SI Appendix*, Figs. S13–S15). Swallowing, another experimental MA event, was tested under various conditions, including after different numbers of chews, various time intervals between swallows, and different liquids swallowed. The LaHMo system successfully visualized the photovoltage data from the various test conditions, demonstrating a clear distinction between the MA of swallowing under different circumstances (*SI Appendix*, Figs. S16–S18). Another MA event used for visualization testing was the performance of different vowel phonemes. The LaHMo system was found to be capable of not only visualizing but also differentiating between 11 different vowel phonemes (*SI Appendix*, Figs. S19–S30). *SI Appendix*, Fig. S31 presents the LaHMo data during the subject's production of different pitches, ranging from G4 to C3, along with the corresponding audio segments. *SI Appendix*, Fig. S32 extends the analysis by comparing head and chest voice production at G4, and further shows the LaHMo data for whispered and loud sounds at C3, all with their respective audio recordings. HM events were used the LaHMo's PD response to motion and the subsequent visualization of the response. Test subjects moved their heads such that their cranial pitch angles were altered, with the LaHMo system successfully detecting and visualizing these motions (*SI Appendix*, Fig. S33).

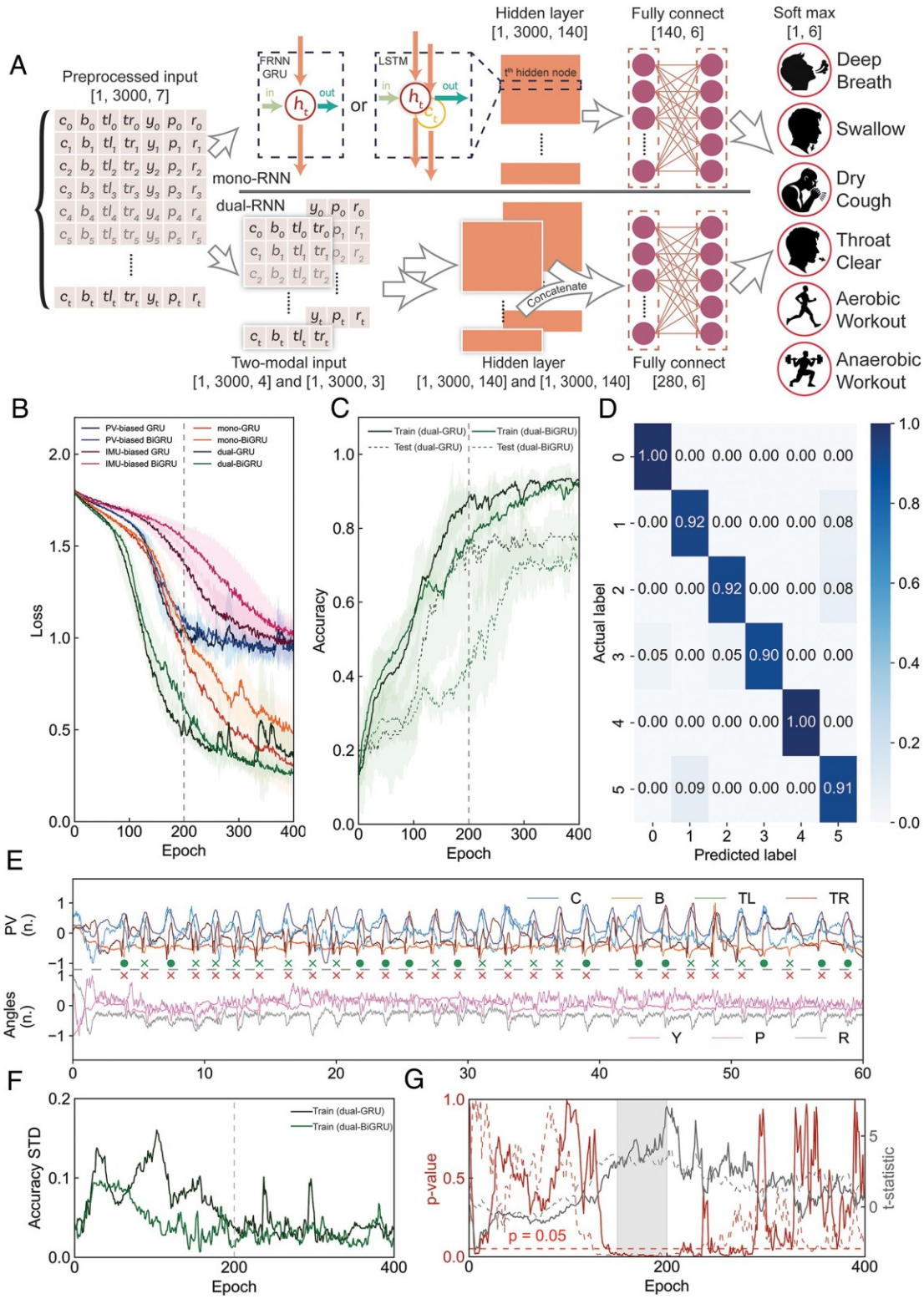


**Fig. 3.** Neural network (NN) classification of the preprocessed windows. (*A*) Flow diagram of AI models highlighting three candidate architectures of RNN. Their distinguishment resides in utilizing mono- and dual-variants (represented by mono-RNN and dual-RNN respectively) of three different RNN architectures, including FRNN, LSTM, and GRU, respectively. For FRNN and GRU, there is only a hidden state ( $h_t$ ) in every hidden layer cell; for LSTM, there is a hidden state ( $h_t$ ) and a cell state ( $_t$ ) in each hidden layer cell. Four NN layers are demonstrated, with the dimension labeled underneath each diagram block. The preprocessed input and the output of a 1-s sample are displayed at the start and end of the flow diagram. (*B*) Loss curves comparison over the course of 400 epochs (performance of GRU) among training of the eight RNNs, including PV-biased RNN, PV-biased BiRNN, IMU-biased RNN, IMU-biased BiRNN, mono-RNN, mono-BiRNN, dual-RNN, and dual-RNN. (*C*) Accuracy curves of training and testing over the course of 400 epochs for the dual-GRU and dual-BiGRU networks. (*D*) Confusion matrix of the dual-GRU and other networks in the preprocessed data. (*E*) Representative test on physiological events detection, involving continuous dry coughing. Green circles label dry cough events in the test set. Green crosses label dry cough in the training set. Red crosses label predicted events with the dual-GRU model. Legends of sensor units: C: Central, B: Bottom, TL: Top Left, TR: Top Right, Y: Yaw, P: Pitch, R: Roll. (*F*) SD of the accuracy curves of the dual-GRU and dual-BiGRU networks for the training dataset over 400 epochs. (*G*) The *P*-values and t-statistics of the null hypothesis (i.e., the dual-GRU does not outperform the dual-BiGRU during the training process) over 400 epochs. Within the shaded area, as the training approaches the ES point, the *P*-values of the hypotheses for both the testing and training datasets drop to the rejection region (at a significance level of 0.05). As such, at the training ES point, statistical analysis suggests a rejection of the null hypothesis, due to the dual-GRU being more robust when encountering different inputs.

To demonstrate the independence of the dual-GRU model in the selection of the training and test sample, a k-fold cross-validation (k = 5) is implemented during the training of the models. The validation is visualized by tracking the STDs of the loss and accuracy of both the training and the testing datasets (the shaded area in Fig. 3 *B* and *C*). A large STD around the training ES point would suggest a poor reproducibility of the model. Fig. 3*F* shows the development of the accuracy STD of dual-GRU and dual-BiGRU in the 5 folds of training, and the accuracy STD and loss STD plots of other mentioned models can be found in *SI Appendix*, Fig. S34. The STD tracking plot shows a significant reduction for both models, suggesting an increase in prediction robustness. Both models also show a steady and low STD around the 200th epoch, suggesting this point is a decent ES point. To compare the performance of the two models, a statistical examination over various data splits (Fig. 3*G*) shows the trajectory of the *P*-value and t-statistic of the null hypothesis, indicating that the dual-GRU shows consistent performance with the dual-BiGRU during the training process. As seen in the shaded area, as the training approaches the ES point, the *P*-values of the hypotheses for both the training and testing datasets drop to the rejection region (at a significance level of 0.05). Therefore, at the training ES point, it is statistically confirmed that the dual-GRU is more robust when encountering different divisions of inputs, with the data ultimately rejecting the null hypothesis.

**Long-Term LaHMo Test.** To validate the LaHMo platform's efficacy in real-world scenarios, we conducted a 30-min on-body test during a basketball game. The test subject wore the LaHMo patch on the anterior neck while performing various activities, including deep breathing, coughing, anaerobic exercises (e.g., shooting the ball), and aerobic exercises (e.g., dribbling and jogging). Fig. 4*A* presents a subset of the raw data collected from this on-body test, with the gray line representing the yaw angle as the representative Euler angle detected by the IMU sensor and the red line representing the photovoltage detected by a representative NIRS sensor. During the 2,000-s recording period, 230 moments were manually marked as occurrences of coughs (71 occurrences, green circles) or noncough events (159 occurrences, blue squares). Fig. 4*B* presents 3-s intervals of the raw data showcasing the correspondence with certain activities executed by the subject during the long-term test, including running, shooting, dribbling, and attempting a layup. *SI Appendix*, Figs. S35 and S36 shows the training performances of the adap-GRU model (40, 41).

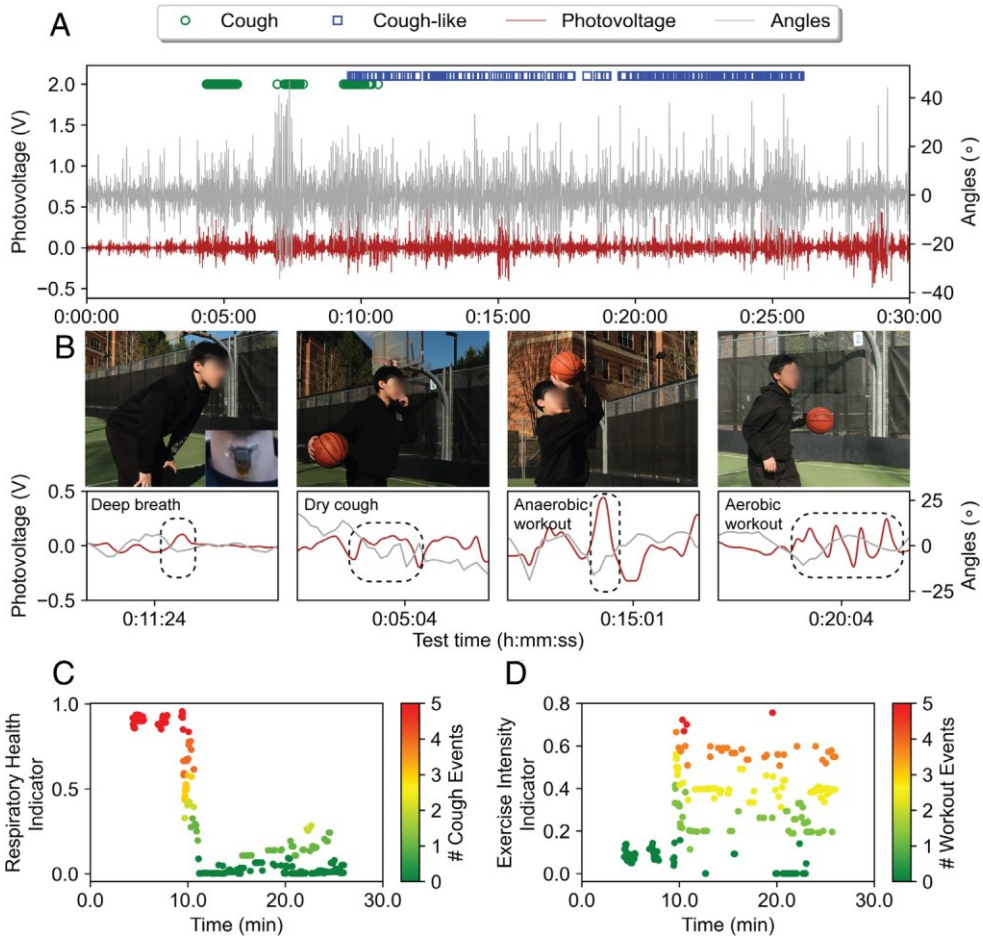


**Fig. 4.** Deployment and analysis of LaHMo during daily activities. (*A*) The representative central (red) and yaw (gray) measurements during a 30-min test during a basketball game. The markers show the manually labeled cough (green circles) and cough-like (blue rectangles) events. The latter contains deep breaths and aerobic and anaerobic exercises during the long test. After data preprocessing, the fine-tuned adap-GRU model produces a real-time prediction based on the 3 s slices. (*B*) Photographs (*Top* row) and corresponding 3 s slices of preprocessed data (*Bottom* row) showing the highlighted activities in the classification algorithm. From *Left* to *Right*: deep breath during rest, dry cough, anaerobic workout (shooting ball), and aerobic workout (dribbling and jogging). The black dashed boxes show the unique features that are considered during the manual label process. (*C*) Calculated respiratory health indicator as a function of time. The datapoint color indicates the number of observed coughs in a 5-s window, that ranges from no cough (green) to 5 coughs per time window (red). (*D*) Calculated exercise intensity indicator as a function of time. The datapoint color indicates the number of observed exercise events in a 5-s window, that ranges from no workout (green) to intensive workouts (red).

*SI Appendix*, Figs. S37 and S38 present the performance of the AI model in action identification over time. These raw predictions enable the calculation of high-level health indicators (Fig. 4 *C* and *D*). Fig. 4*C* presents the respiratory health indicator, defined as the average prediction score of cough events within a 5-s window, accompanied by the number of observed cough events in that period. Fig. 4*D* illustrates the exercise intensity indicator, determined by the combined average prediction scores of anaerobic and aerobic workouts within a 5-s window, along with the number of observed workout events. These results allow us to quantitatively assess the relationship between the subject's respiratory health condition and their exercise intensity during the workout. By comparing the respiratory health indicator with the exercise intensity indicator, we can evaluate whether increased exercise intensity correlates with a decline in respiratory health or vice versa. This quantitative analysis provides valuable insights into how physical activity impacts respiratory function, helping to identify potential issues and optimize training and health monitoring protocols for individuals based on their specific needs and conditions.

**Validation with Gold Standard and Monte Carlo Simulation.** To understand the underlying correspondence between the signals collected from LaHMo and the muscular movements of the neck, a time-resolved Monte Carlo (MC) simulation is utilized to present a view of both internal muscular movements and corresponding optical modulations in the laryngeal (42–47). In addition to the simulation, we performed gold-standard validation using EMG, where LaHMo was compared against EMG recordings of the thyrohyoid membrane, cricothyroid muscle, and suprahyoid muscles during controlled swallowing events. This comparison revealed a high degree of signal alignment, confirming LaHMo's ability to track swallowing movements in real time, corroborating the simulation with physiological measurements. A videostroboscopy (VSS) test further confirmed the alignment of the LaHMo data with the activity of vocal folds during the production of natural musical scales using chest voice and falsetto, respectively.

In each MC simulation experiment, $10^7$ photon wave packets are launched into a predefined voxel space, and the trajectory and weight of each wave packet along all the time steps are recorded (*SI Appendix*, Note S2). Fig. 5*A* shows the laryngeal region with contour outlines defining the voxel space emulated in the simulation. The image depicts the LP of the throat, that defines sensing areas of the LaHMo patch. Accompanying this is a cross-sectional model of the layered tissue at the site: the epidermis, dermis, subcutaneous fat, and skeletal muscle. A close-up video is first recorded (Movie S2) to show a frame-by-frame profile change of the laryngeal area. The contour of the laryngeal prominence (LP) is manually extracted from the video for every frame and is modeled in the voxel space. Finally, a series of parallel boundaries inside the voxel space is generated to represent the borders between the epidermis, dermis, subcutaneous fat, and skeletal muscles. The LaHMo placement and light emission, both on a tissue surface and the LP, are respectively represented by *SI Appendix*, Figs. S39 and S40. During each physiological activity (deep breath, dry cough, throat clearing, and swallowing) in this simulation, the motion will be mainly induced by the vertical and horizontal displacement of the LP.

Fig. 5*B* presents a three-dimensional graph of three dependent variables, describing the neuromuscular activity in the laryngeal region: the logarithm of the fluence at the LaHMo patch's CP (central photodiode), the height of the LP (mm), and the vertical displacement (mm) of the LP from a set baseline throughout the Monte Carlo simulation. The logarithm of the fluence is the calculated brightness of the tissue at the site of the CP during the simulation. The LP height is the height of the LP's peak relative to the baseline set at the surface of the throat. The vertical displacement, finally, is the location of the LP's peak relative to the vertical midpoint of the throat. A color bar enables a more streamlined interpretation of the figure, indicating the value of the logarithm of the fluence corresponding to the colored region on the three-dimensional graph. The cross-sectional profiles in Fig. 5*C* and *SI Appendix*, Fig. S41 show the locations (blue triangles) and corresponding emitted near-infrared light (purple extrusions) of 2 LEDs (Central and Bottom ones corresponding to Fig. 2*A*) from the deployed LaHMo. Fig. 5*C* shows three cross-section profiles of the emitted light per physiological activity, representing the initiation stage, peak stage, and ending stage, respectively. Fig. 5*C* also provides a comparison between the average photovoltage response of the central and bottom PDs and their simulated counterparts, with the former represented by solid lines and the latter represented by dashed lines and crosses. Orange vertical dashed lines on the graphs designate the times lining up with the respective cross-sectional profiles of the Monte Carlo simulation.

To quantitatively assess the agreement between the Monte Carlo (MC) simulated results and the actual measured signals for the deep breath event, we performed a cross-correlation analysis using a sliding window approach. The MC simulated signals and the measured signals were compared for both the central and bottom channels (*SI Appendix*, Fig. S42). In this analysis, the signals from both measurements and MC simulations are first normalized before being matched on the time axis to compensate for the unit mismatch between fluence (results of MC simulation) and photovoltage (measurements of PD). The cross-correlation is calculated after the normalization and best matching of the segment and the MC simulated signal. Overall, the central channels for the four activities show higher best correlations at around zero lag (0.77 for deep breath, 0.80 for dry cough, 0.75 for throat clearing, and 0.63 for swallowing) indicating a strong similarity. The best correlations (0.79 for dry cough, 0.29 for dry cough, 0.36 for throat clearing, and 0.50 for swallowing) for bottom channels are less significant but still ample to show a similarity. These findings validate the accuracy of the MC simulation in capturing the underlying muscle activities during different physiological events and support the feasibility of using MC simulations to investigate the relationship between the detected signals and the corresponding physiological events.

To validate the LaHMo's data with gold standard, a simultaneous EMG test is performed where the activity patterns of the thyrohyoid muscle, cricothyroid muscle, and suprahyoid muscles during a swallowing event are recorded (Fig. 5 *D*–*F*). The validation experiment involved three distinct swallowing events monitored simultaneously by both EMG and LaHMo over a 10-s interval. The EMG data and LaHMo data are shown in Fig. 5 *E* and *F*, highlighted in orange boxes for each swallow. The results demonstrate a high level of signal alignment between the EMG and LaHMo across all monitored muscle groups, confirming that LaHMo can track the muscle activities associated with swallowing. To further extend this validation, a proof-of-concept videostroboscopy (VSS) experiment is performed that measured LaHMo's ability to track vocalization, particularly pitch modulation in chest voice and falsetto. The VSS recording, presented in *SI Appendix*, Fig. S44, was obtained from an authentic external source (48), and provided a visual confirmation of the vocal fold dynamics. *SI Appendix*, Fig. S44 *A* and *C* depict LaHMo data as the subject produced natural musical scales ranging from C3 to C4 using

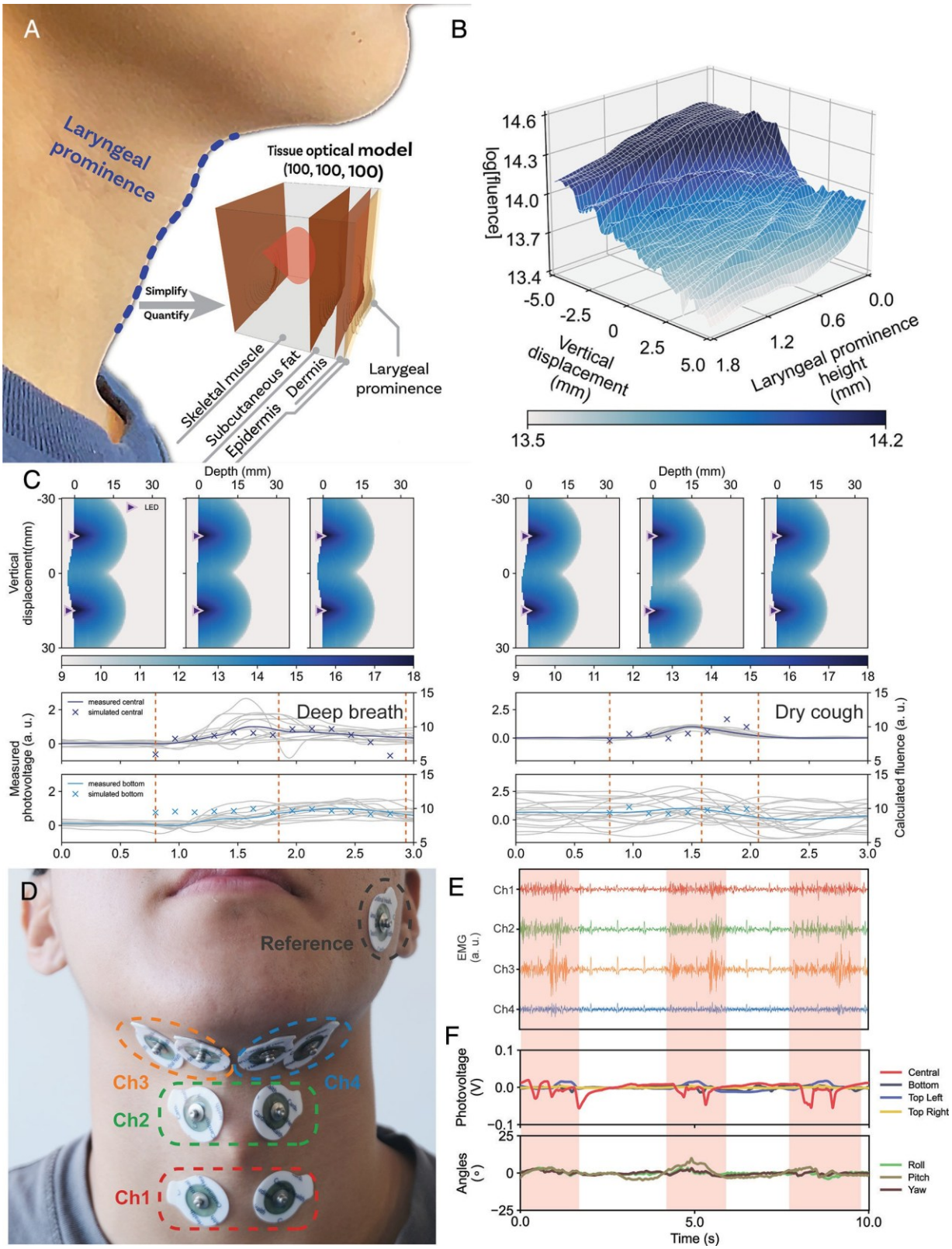


**Fig. 5.** Monte Carlo simulation to validate the correlation between signals collected from LaHMo patch and corresponding muscular movements from the neck. (*A*) A photographic depiction of the LP, the targeted sensing area of the LaHMo patch. Video recordings of the anterior neck during various activities (deep breath, dry cough, throat clearing, and swallowing) yield measurements of its contour movements for comparison with simulation results. *Inset*: a cross-sectional model of the layered tissue at the sensing site, which consists of the epidermis, dermis, subcutaneous fat, and skeletal muscle (from outside inward). (*B*) A 3D contour plot showing the simulation results on the logarithm of the fluence corresponding to responses from the central photodiode of a LaHMo patch. The height of the LP (the distance between the LP's peak and the surface of the throat) and the LP's vertical displacement (the location of the LP's peak relative to the midpoint of the throat) over the experiment. The logarithm of fluence is the calculated brightness of the tissue in the operational area. The LP height and the vertical displacement are shown on the bottom plane. (*C*) Simulation results on the cross-sectional profiles of LED illumination from a LaHMo patch into the neck and their accompanying measured photovoltage and calculated fluence data during the deep breath and dry cough actions. To facilitate a practical visualization of the effects of the actions, there are three cross-section profiles per physiological action: at the start point, the point of the greatest change in the measurement, and the endpoint, respectively. (*D*) Placement of the electrode of four EMG channels and the reference. (*E*) Acquired EMG signals at three different swallow events (highlighted with orange boxes) in a 10-s interval. (*F*) Acquired LaHMo data at the corresponding time interval.

chest voice, and C4 to C5 using falsetto. The audio recordings of these events, shown in *SI Appendix*, Fig. S44 *B* and *D*, correlate the vocal performance with the muscle activity captured by LaHMo. *SI Appendix*, Fig. S44 *E–H* provides VSS slices during these vocalizations, showing the distinct movement of the corniculate cartilages (highlighted by green dashed circles). The VSS confirms the posterior movement of the corniculate cartilages during falsetto, which aligns with the optical data recorded by LaHMo, further validating the platform's ability to monitor vocal fold dynamics.

This combination of MC simulations and gold standard measurements, including EMG and VSS, validates the operational robustness of LaHMo, demonstrating that the device accurately captures physiological events such as swallowing and vocalization, while offering insight into both swallowing-related muscular movements and dynamic changes during phonation.

## Discussion

In this study, we present the LaHMo platform, a wearable system that leverages near-infrared spectroscopy (NIRS) and inertial measurement unit (IMU) sensors with a dual-modality AI algorithm to continuously monitor laryngeal muscle activity with high precision. The LaHMo platform exhibits significant potential in providing a direct assessment of the physiological activities of extrinsic laryngeal muscles, such as the sternohyoid, thyrohyoid, and suprahyoid, which are integral to laryngeal positioning and stabilization. Additionally, it offers indirect insights into the behavior of intrinsic laryngeal muscles, like the thyroarytenoid and cricothyroid, which are crucial for vocal fold modulation and phonation (49). This dual capability enables the platform to enhance the understanding and treatment of conditions such as dysphonia, dysphagia, post-COVID dry cough, and dystussia by offering a comprehensive view of laryngeal muscle function and its impact on these disorders. The developed dual-GRU model exhibited superior performance compared with the other 24 conventional RNN architectures, demonstrating its ability to effectively synergize NIRS and IMU data and accurately classify muscle activity and head motion events. Both the long-term on-body tests and Monte Carlo simulations further validate the efficacy of the LaHMo platform, highlighting its practical potential for real-world applications. The developed adaptation network (adap-GRU) allows for AI-model individualization without extensive training for target users, making the LaHMo platform more accessible and user-friendly.

Finally, the LaHMo platform is designed to offer valuable insights into daily behaviors of laryngeal muscles, such as swallowing and breathing, by continuously monitoring collective muscle activities in a noninvasive manner. Its long-term wearability and noninvasive tracking lead to its promising utility more on preliminary clinical screening for hospital admission and proactive diagnosis for critical early-stage indicators, but the limited spatial quantification and structural correspondence in the analyzed signals make the system less useful for deep mechanistic analysis of a singular muscle function. Specifically, during the examination of the swallowing process, the LaHMo platform effectively tracks hyolaryngeal elevation and tongue movements, and the preliminary evidence from the IDDSI level tests (*SI Appendix*, Fig. S46) also suggests that the platform can monitor and differentiate tongue movement across various bolus viscosities, providing valuable real-time biofeedback for initial clinical screening and rehabilitation tracking. Additionally, for the respiration, the LaHMo platform cannot comprehensively describe the complex dynamics of breathing, which primarily involve the diaphragm and intercostal muscles. Therefore, while it can provide insights into basic breathing behaviors, such as distinguishing between oral and nasal breathing (*SI Appendix*, Fig. S47), it is not equipped to offer a comprehensive analysis of respiratory function. Moreover, while long-term tests and simulations conducted in controlled environments suggest the potential efficacy of the LaHMo platform for real-world applications these findings are preliminary. Simulations and lab tests, although useful, cannot fully replicate the complexities encountered in clinical trials with human subjects, where factors like patient variability and long-term device performance play critical roles. Future studies may focus on validating the system's performance in larger and more diverse patient populations, including those with specific NMDs. Additionally, the integration of the LaHMo platform with other diagnostic tools and treatment modalities may hold great promise to improve patient outcomes and enhance clinical decision-making in treating muscular disorders.

## Methods

**Device Design and Components.** The outline of the three flexible PCB (fPCB) islands and two serpentine hinges are defined in Autodesk AutoCAD 2023 before being incorporated into the fPCB design. The fPCB schematic and board layout are finished using Altium Designer (version 24.1.2). The bill of materials (BOM) can be found in *SI Appendix*, Table S1.

**Device Fabrication.** Panels of fPCB were manufactured according to international standards ISO 9001:2005 and IPC. Solder paste is dispensed with a desktop PCB prototype machine (V-One, Voltera). The components are populated manually.

**Data Collection.** The device is secured to make sure the top and bottom NIRS sensors are above and below the subject's laryngeal prominent, respectively. Three of the authors participated in one or more of the 4 tests (Details in *SI Appendix*, Table S2). The data are collected via BTViz. Additional operating information can be found in *SI Appendix*, Note 3. The on-body evaluation of the LaHMo was performed in compliance with the protocol that was approved by the institutional review board at the University of North Carolina, Chapel Hill (study number 22-0163).

**Data Analytics.** The real-time data preprocessing procedures during the tests are deployed on a personal computer running Linux (Manjaro), including two Butterworth filters, one peak finding function, and one slice stacking algorithm. The detailed calculations can be found in *SI Appendix*, Note 4. All the above-mentioned neural networks are built with the PyTorch package (version 2.0.0, based on CUDA 12.1 platform). The network dimensional parameters of the 24 tested RNN variants and the adap-GRU can be found in *SI Appendix*, Table S3. The training and validation were conducted in Visual Studio Code (version 1.86) environment embedded with Python 3.10.11.

**Monte Carlo Simulation.** The platform of the MC simulation used in this project is MCXLAB v2020 (1.8 - Furious Fermion), an open-source light transport simulator. Two MC optical simulations are performed: normal status (NS) and bump translate (BP). The detailed performances of these simulations can be found in *SI Appendix*, Note 2.

**EMG Validation Test.** The EMG validation test starts by placing 9 electrodes (Kendall™, CardinalHealth) onto the subject's neck at the labeled locations. Eight electrodes are connected to channel 1 to 4 of a PowerLab 16/35 data acquisition system (ADInstruments), and the last electrode is connected to the external ground port. The data acquisition is performed by the LabChart 7 software. For all the input channels, the sample frequency is set to 100 kHz. On all the input differential amplifiers, a bandpass filter is added, with a 1 Hz low cutoff and a 50 Hz high cutoff. A LaHMo patch is applied after all electrodes are placed. The subject uses a straw to drink a mouthful of water to prevent redundant mouth movement before swallowing the liquid naturally.

**Data, Materials, and Software Availability.** All raw data, analysis code, firmware code data have been deposited in Zenodo (50).

**ACKNOWLEDGMENTS.** This work was supported by start-up funds from University of North Carolina at Chapel Hill and the fund from NSF (award # ECCS-2139659).Research reported in this publication was also supported by the National Institute of Biomedical Imaging and Bioengineering at the NIH under award number 1R01EB034332-01. This work is also supported by NeuroSpark Awards from UNC Neuroscience Center and Translational Research Grant from North Carolina Biotechnology Center.

1. B. M. Morrison, Neuromuscular diseases. *Semin. Neurol.* **36**, 409–418 (2016).
2. L. Rose *et al.*, Trends in incidence, prevalence, and mortality of neuromuscular disease in Ontario, Canada: A population-based retrospective cohort study (2003–2014). *PLoS One* **14**, e0210574 (2019).
3. C. Klug *et al.*, Disease burden of spinal muscular atrophy in Germany. *Orphanet J. Rare Dis.* **11**, 58 (2016).
4. E. Landfeldt *et al.*, Mortality cost of Duchenne muscular dystrophy. *Neurology* **83**, 529–536 (2017).
5. A. A. Rodríguez *et al.*, Diseases costs and impact of the caring role on informal carers of children with neuromuscular disease. *Int. J. Environ. Res. Public Health* **18**, 2991 (2021).
6. A. Putcha, T. Nguyen, R. Smith, R. Choffin, W. Bai, Intelligent systems for muscle tracking: A review on sensor-algorithm synergy. *Adv. Intell. Systems* **5**, 2200351 (2023).
7. J. Kim, A. S. Campbell, B. E. F. de Ávila, J. Wang, Wearable biosensors for healthcare monitoring. *Nat. Biotechnol.* **37**, 389 (2019).
8. K. H. Lee *et al.*, Mechano-acoustic sensing of physiological processes and body motions via a soft wireless device placed at the suprasternal notch. *Nat. Biomed. Eng.* **4**, 148–158 (2019).
9. X. Ni *et al.*, Automated, multiparametric monitoring of respiratory biomarkers and vital signs in clinical and home settings for COVID-19 patients. *Proc. Natl. Acad. Sci. U.S.A.* **118**, e2026610118 (2021).
10. M. Zhu *et al.*, "Contraction patterns of facial and neck muscles in speaking tasks using high-density electromyography" in *Proceedings of the International Conference on Sensing Technology, ICST2019* (EEE, Sydney, Australia, 2019).
11. A. Sasegbon, S. Hamdy, The anatomy and physiology of normal and abnormal swallowing in oropharyngeal dysphagia. *Neurogastroenterology Motility* **29**, e13100 (2017).
12. I. Hertrich, S. Dietrich, H. Ackermann, The role of the supplementary motor area for speech and language processing. *Neurosci. Biobehav. Rev.* **68**, 602–610 (2016).
13. A. Aliverti, The respiratory muscles during exercise. *Breathe* **12**, 165–168 (2016).
14. M. Kunduk, D. S. Fink, A. J. McWhorter, Primary muscle tension Dysphonia. *Curr. Otorhinolaryngol. Rep.* **4**, 175–182 (2016).
15. L. R. Carucci, M. Ann Turner, Dysphagia revisited: common and unusual causes. *Radiographics* **35**, 105–122 (2015).
16. W. J. Song *et al.*, Confronting COVID-19-associated cough and the post-COVID syndrome: Role of viral neurotropism, neuroinflammation, and neuroimmune responses. *Lancet Respir. Med.* **9**, 533–544 (2021).
17. P. V. Dicpinigaitis, B. J. Canning, Is there (will there be) a post-COVID-19 chronic cough? *Lung* **198**, 863–865 (2020).
18. S. Ebihara, H. Sekiya, M. Miyagi, T. Ebihara, T. Okazaki, Dysphagia, dystussia, and aspiration pneumonia in elderly people. *J. Thorac. Dis.* **8**, 632 (2016).
19. A. Ghosh *et al.*, "On automatizing recognition of multiple human activities using ultrasonic sensor grid" in *2017 9th International Conference on Communication Systems and Networks, COMSNETS 2017*, N. Ganguly, Ed. (IEEE, Bengaluru, India, 2017), 488-491. 10.1109/COMSNETS.2017.7945440.
20. A. Huang, Y. Ono, "Estimation of wrist flexion angle from muscle thickness changes measured by a flexible ultrasonic sensor" in *3rd IEEE EMBS International Conference on Biomedical and Health Informatics, BHI 2016*, S. Wong, Ed. (IEEE, Las Vegas, Nevada, 2016), pp. 188-191. 10.1109/BHI.2016.7455866.
21. E. Yeung, I. Almohimeed, Y. Ono, "Estimation of tissue thickness changes due to electrical muscle stimulation using wearable ultrasonic sensor in pulse echo mode" in *Proceedings of IEEE Sensors*, F. Labeau, Ed. (IEEE, Montreal, Canada, 2019).
22. F. Xie *et al.*, Development of a wireless multichannel near-infrared spectroscopy sensor system for monitoring muscle activity. *IEEE Sens J.* **22**, 22714-22724 (2022).
23. M. Sikora, S. Paszkiel, Muscle activity measurement using visible light and infrared. *IFAC-PapersOnLine* **52**, 329–334 (2019).
24. M. Lacerenza *et al.*, Wearable and wireless time-domain near-infrared spectroscopy system for brain and muscle hemodynamic monitoring. *Biomed. Optics Express* **11**, 5934-5949 (2020).
25. R. H. Chowdhury *et al.*, Surface electromyography signal processing and classification techniques. *Sensors* **13**, 12431-12466 (2013).
26. T. Roland, K. Wimberger, S. Amsuess, M. F. Russold, W. Baumgartner, An insulated flexible sensor for stable electromyography detection: Application to prosthesis control. *Sensors* **19**, 961 (2019).
27. N. Akhlaghi *et al.*, Real-time classification of hand motions using ultrasound imaging of forearm muscles. *IEEE Trans. Biomed. Eng.* **63**, 1687–1698 (2016).
28. R. J. Cotton, J. Rogers, "Wearable monitoring of joint angle and muscle activity" in *IEEE International Conference on Rehabilitation Robotics*, R. Riener, Ed. (IEEE, Toronto, Canada, 2019), pp. 258-263.
29. W. Wei, K. Kurita, J. Kuang, A. Gao, "Real-time 3D arm motion tracking using the 6-axis IMU sensor of a smartwatch" in *2021 IEEE 17th International Conference on Wearable and Implantable Body Sensor Networks, BSN 2021*, P. Bonato, Ed. (IEEE, Athens, Greece, 2021).
30. S. Yacoub, A. H. Al-Timemy, Y. Serrestou, K. Raoof, "Hand movements analysis with acoustic myography signals" in *Proceedings of the 2022 5th International Conference on Advanced Systems and Emergent Technologies, IC_ASET 2022*, A. B. Amor, Ed. (IEEE, Hammamet, Tunisia, 2022), pp. 228–232. https://doi.org/10.1109/IC_ASET53395.2022.9765920.
31. Y. Takei, R. Aoki, T. Kobayashi, T. Takahata, I. Shimoyama, Mechanomyogram measurement by lead zirconate titanate-based acoustic sensor. *Jpn. J. Appl. Phys.* **57**, 11UD09 (2018).
32. C. Meagher *et al.*, New advances in mechanomyography sensor technology and signal processing: Validity and intrarater reliability of recordings from muscle. *J. Rehabil. Assist. Technol. Eng.* **7**, 2055668320916116. 10.1177/2055668320916116.
33. Y. Liu *et al.*, Skin-interfaced deep-tissue sensing patch via microneedle waveguides. *Adv. Mater. Technol.* **7**, 2200468 (2022).
34. A. P. Dumont, Q. Fang, C. A. Patil, A computationally efficient Monte-Carlo model for biomedical raman spectroscopy. *J. Biophotonics* **14**, e202000377 (2021).
35. S. Patel, H. Park, P. Bonato, L. Chan, M. Rodgers, A review of wearable sensors and systems with application in rehabilitation. *J. Neuroeng. Rehabil.* **9**, 21 (2012).
36. J. Kim, A. S. Campbell, B. E. F. de Ávila, J. Wang, Wearable biosensors for healthcare monitoring. *Nat. Biotechnol.* **37**, 389–406 (2019).
37. L. S. Liu *et al.*, Design and test of a low-power acceleration sensor with Bluetooth Low Energy on ear tags for sow behaviour monitoring. *Biosyst. Eng.* **176**, 162–171 (2018).
38. Y. Ma, Q. Chang, H. Lu, J. Liu, Reconstruct recurrent neural networks via flexible sub-models for time series classification. *Appl. Sci.* **8**, 630 (2018).
39. Y. Ma, M. Hu, Q. Chang, H. Lu, "Random projection recurrent neural networks for time series classification" in *Proceedings of 2018 IEEE 8th International Conference on Electronics Information and Emergency Communication, ICEIEC 2018*, W. Li, Ed. (IEEE, Beijing, China, 2018), pp. 40-43. https://doi.org/10.1109/ICEIEC.2018.8473552.
40. Y. Kim, D. Cho, K. Han, P. Panda, S. Hong, Domain adaptation without source data. *IEEE Trans. Artif. Intell.* **2**, 508–518 (2021).
41. E. Othman *et al.*, Domain adaptation network for cross-scene classification. *IEEE Trans. Geosci. Remote Sensing* **55**, 4441–4456 (2017).
42. L. He, J. Li, C. Sun, Y. Lu, Y. Dong, "GPU-accelerated Monte Carlo simulation for PET imaging (Part I): Validation of imaging physics simulation" in *2023 IEEE Nuclear Science Symposium, Medical Imaging Conference and International Symposium on Room-Temperature Semiconductor Detectors (NSS MIC RTSD)*, V. Sossi, Ed. (IEEE, Vancouver, Canada, 2023).
43. Y. Tachibana, T. Duval, T. Obata, Monte Carlo simulator for diffusion-weighted imaging sequences. *Mag. Reson. Med. Sci.* **20**, 222–226 (2021).
44. S. Yan, S. L. Jacques, J. C. Ramella-Roman, Q. Fang, Graphics-processing-unit-accelerated Monte Carlo simulation of polarized light in complex three-dimensional media. *J. Biomed. Opt.* **27**, 083015 (2022). 10.1117/1.JBO.27.8.083015.
45. Q. Fang, S. Yan, MCX Cloud—a modern, scalable, high-performance and in-browser Monte Carlo simulation platform with cloud computing. *J. Biomed. Opt.* **27**, 083008 (2022). 10.1117/1.JBO.27.8.083008.
46. S. Yan, Q. Fang, Hybrid mesh and voxel based Monte Carlo algorithm for accurate and efficient photon transport modeling in complex bio-tissues. *Biomed. Optics Express* **11**, 6262–6270 (2020).
47. Q. Fang *et al.*, Monte Carlo simulation of photon migration in 3D turbid media accelerated by graphics processing units. *Optics Express* **17**, 20178–20190 (2009).
48. "Singing Vocal Folds." YouTube, uploaded by ualbertaslp, 13 April 2011. https://www.youtube.com/watch?v=xYT1GG3fUdw.
49. Z. Zhang, J. Yin, The role of the thyroarytenoid muscle in the regulation of prephonatory glottal opening. *J. Acoust. Soc. Am.* **133**, 3601–3601 (2013).
50. Y. Liu *et al.*, LaHMo. Zenodo. https://doi.org/10.5281/zenodo.13835256. Deposited 24 September 2024.